Gravity wave vertical wind distributions shape homogeneous ice nucleation in tropical tropopause layer cirrus

Bernd Kärcher[1]

[1]German Aerospace Center (DLR), Institute for Atmospheric Physics, Oberpfaffenhofen, Germany

Correspondence: Bernd Kärcher (bernd.kaercher@dlr.de)

Abstract. Internal gravity waves have a profound impact on the nucleation of cirrus ice crystals in the stably stratified upper troposphere. Cloud models require the use of parameterization schemes that represent gravity wave-induced variability in vertical wind speeds with high fidelity. Accounting for such variability in microphysical models is a stringent test of their ability to accurately simulate ice nucleation events in cirrus. However, such schemes are sparse and have not been characterized in detail. This study presents a comparative analysis of how several wave-cirrus parameterizations impact the formation of tropical tropopause layer cirrus by evaluating simulated distributions of homogeneously nucleated ice crystal number concentrations against the statistic based on long-duration superpressure balloon measurements. Fluctuation distributions, temporal autocorrelations, and power spectra are analyzed for both measurements and parameterizations. Driven by these inputs, microphysical simulations yield broad ice number distributions with consistent results between the balloon-borne data and synthetic exponential vertical wind speed parameterizations. Moderate discrepancies between these distributions fall within the uncertainty range of independent microphysical models. These differences are primarily attributable to the data filtering necessary to remove non-geophysical artifacts from the balloon measurements, alongside spectral power mismatches across the buoyancy frequency. To substantially improve wave-cirrus parameterizations in process-based and global models, future research should prioritize enhancing the representation of non-orographic gravity wave forcing as a function of distance from source regions and within wave-trapping environments.

1 Introduction

The dynamical forcing of vertical wind speeds and temperature across a wide range of spatial and temporal scales exerts a strong impact on homogeneous freezing events (HFEs) in cirrus clouds, and thus on the competition between homogeneous and heterogeneous ice nucleation in aerosol-cirrus interactions (Kärcher, 2017). Without reducing associated uncertainties, there is little hope to more tightly constrain predictions of cirrus lifecycles and improve estimates of their climatic impact.

Cloud-scale motions are not resolved in global models. For this reason, microphysics must be driven by parameterizations for the unresolved cloud dynamical forcing (Morrison et al., 2020). While most large-scale models include a representation of turbulence forcing to cover sub-km spatial scales, the dynamics of stratiform cirrus clouds at the mesoscale below about $100\,\mathrm{km}$—the domain of Large-Eddy Simulations—is only poorly, if at all, resolved. At the mesoscale, vertical air motion variability is driven by ever-present internal gravity waves (GWs). With regard to GWs, the meso-γ scale at the border to the

outer turbulence length scale ($10-100$ m) is important, as the short period components of these waves coincide with nucleation time scales and thus provide the main forcing of ice nucleation in cirrus (Kärcher and Ström, 2003; Hoyle et al., 2005; Dinh et al., 2016; Jensen et al., 2016a; Corcos et al., 2023).

Several global models parameterize the effect of orographic gravity wave forcing on cirrus formation (Dean et al., 2007; Joos et al., 2008; Lyu et al., 2025). By contrast, little progress has been made to account for cloud-scale updraft speeds and associated temperature fluctuations due to non-orographic GWs. One climate model (Wang and Penner, 2010) incorporates a link between such fluctuations and cirrus formation, but the prescribed fluctuations are not aware of changing atmospheric conditions influencing GW propagation and properties (Kärcher and Podglajen, 2019, section 5.1).

Direct experimental information on GW properties is available from long-duration, quasi-Lagrangian superpressure balloon (SPB) measurements in the tropics and polar regions, showing that GW-induced vertical wind speed and resulting temperature fluctuations can be described as a stochastic process (Podglajen et al., 2016). Fluctuations due to GWs determine the formation (Jensen et al., 2026) and lifetimes (Corcos et al., 2026) of thin cirrus clouds in the tropical tropopause layer (TTL). These ice clouds show high frequencies of occurrence in the TTL (Wang et al., 1996; Lesigne et al., 2024) and play a critical role in deyhdrating air masses at entry to the stratosphere (Randel and Jensen, 2013).

A broad GW frequency spectrum is present at upper tropospheric (cirrus) altitudes due to a multitude of wave sources and propagation conditions set by thermal and wind fields (van Zandt, 1982). In the present study, the focus lies on non-breaking, short-period GWs with intrinsic frequency components up to the buoyancy (Brunt-Väisälä) frequency, N. High frequency GWs are closely related to tropical deep convection (Corcos et al., 2021) and are therefore of special importance for the formation of TTL cirrus *via* homogeneous freezing of aqueous solution droplets (Jensen et al., 2026). Low frequency atmospheric waves with intrinsic periods of hours or longer have a negligible impact on HFEs due to their comparatively low cooling and heating rates.

The present study employs SPB measurements of GW properties in the TTL from campaigns in the France-U.S. collaborative Stratéole-2 project (Haase et al., 2018) together with stochastic models (wave-cirrus parameterizations, WCPs) that represent GW-induced fluctuations in large ensemble microphysical simulations. The main objective is to evaluate the ability of several candidate WCPs—each with distinct spectral features and fluctuation distributions—to predict probability distributions of homogeneously nucleated ice crystal number concentrations in TTL cirrus. The work presented here critically assesses how well the WCPs can drive process-based cirrus simulations and thus provides guidance for future developments of more advanced WCPs. In this way, the present study provides new knowledge that could help improve model predictions of how air becomes dehydrated before entering the stratosphere.

Jensen et al. (2026) investigated relationships between the properties of GW-induced vertical wind speed fluctuations and statistics of homogeneously nucleated ice crystal number concentration near the cold point tropopause. The present study extends this work by investigating stationary statistical properties of the fluctuations in broader terms and by performing a comparative analysis of ice number statistics with the help of additional WCPs and an independently developed microphysical simulation code. Section 2 introduces and analyses the SPB measurements. Section 3 presents the microphysical model alongside its coupling with the GW forcing. Section 4 describes the stochastic WCP approaches and their intersections with the SPB

data. Section 5 presents and discusses effects of GW activity on TTL cirrus formation. Section 6 summarizes the main findings and elaborates on future avenues of research that follow from this work.

2 Superpressure balloon data analysis

2.1 Time series of vertical wind speed fluctuations

This study employs SPB measurements of air pressure in the TTL near the cold point tropopause, from which time series of vertical displacements and associated wind speed fluctuations, $w'(t)$, were derived from the pressure measurements (Jensen et al., 2026). In the tropical band, the variance of these fluctuations, σ_w^2, is strongly correlated with convective activity and decreases with distance from convection (Corcos et al., 2021). Here, the time series is considered to be stationary, *i.e.*, the true statistical moments and frequency distributions of the fluctuations do not depend on the time the data were taken.

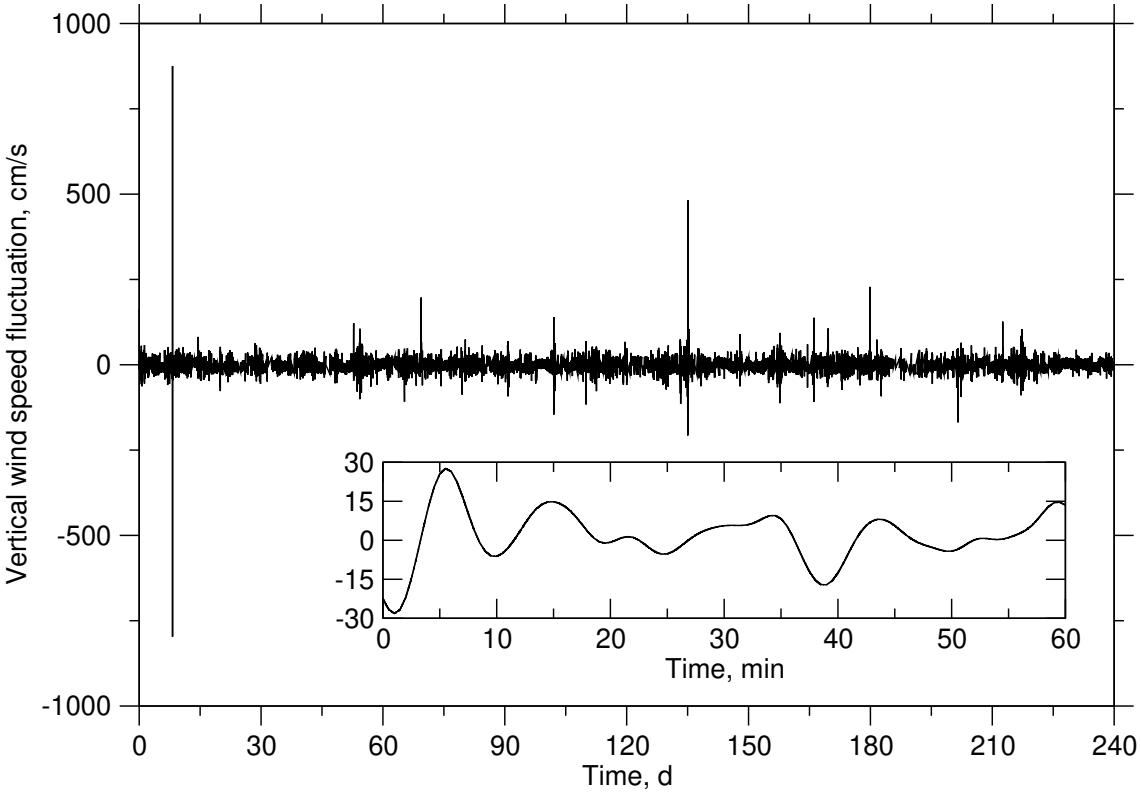

Figure 1. Time series of N-filtered vertical wind speed fluctuations from SPB observations in the TTL from the Stratéole-2 project. The data resolution is $30\,\mathrm{s}$. The inset shows a short sequence of the time series with fluctuations interpolated at $0.1\,\mathrm{s}$, the time step used in the nucleation simulations.

Filters were used to select the range of intrinsic GW periods (equivalently, angular frequencies ω) from the time series, bounded by 1 day and the buoyancy period, $t_\mathrm{b} = 2\pi/N$. The removal of periods longer than 1 day is not important for this study, but the analysis of wind data in the high frequency range is compromised to a degree by mechanical, oscillatory motions of the balloons (Wilson et al., 2023). A Bessel band pass filter was applied with a cut-off frequency of $N = 0.0233\,\mathrm{rad\,s^{-1}}$ ($t_\mathrm{b} \simeq 4.5\,\mathrm{min}$) to limit the impact of the balloon oscillations (Corcos et al., 2023). The high frequency filtering also removes fluctuations from turbulence with frequencies above N.

Measurement data from all TTL flights were combined into a single continuous dataset. Data points sampled during depressurization events or while the balloons were still rising were removed prior to analysis. Figure 1 displays the remaining w'-time series, with a total duration of about 241.36 days, equivalent to $695{,}104$ data points in total for the temporal data resolution of $30\,\mathrm{s}$. The standard deviation is $\sigma_w = 0.12\,\mathrm{m\,s^{-1}}$ and about $0.1\,\%$ of all data have values $> 1\,\mathrm{m\,s^{-1}}$. Several massive perturbations produce very large updraft speeds up to $8.78\,\mathrm{m\,s^{-1}}$, comparable to strong mountain (lee) wave events and indicative of intermittency caused by GWs, *i.e.*, the appearance of sudden bursts in atmospheric GW activity.

2.2 Distribution of fluctuation amplitudes

Figure 2 shows that the w'-fluctuations approximately follow a double-sided exponential statistic (Laplacian), defined as a probability (P) density function:

$$\frac{dP}{dw'} = \frac{1}{2b}\exp -\Big(\frac{|w'|}{b}\Big)\,, \tag{1}$$

where $b = \sigma_w/\sqrt{2}$ is the scale parameter of the distribution, whose mean value is zero. The SPB distribution decays approximately exponentially and is almost symmetric, indicating extensive sampling of w' fluctuations, both in magnitude and sign. The effect of high frequency filtering on the distribution are shown in Podglajen et al. (2016, Fig. 2).

The Laplacian introduces more large-amplitude fluctuations (outside $3\sigma_w$) than its Gaussian counterpart in which fluctuations with amplitudes exceeding $\pm 0.5\,\mathrm{m\,s^{-1}}$ are practically absent. Laplacian distributions of w' are also seen in aircraft measurements at midlatitudes (*e.g.*, Kärcher and Ström, 2003; Jensen et al., 2013). Stronger intermittency features can be modeled by using double-sided, stretched exponential w'-distributions (Podglajen et al., 2016, Supporting Information, Fig. S3). Indeed, closer inspection of the far wings of the distributions in Fig. 2 suggests that the Laplacian may underestimate extreme fluctuations exceeding $\pm 1\,\mathrm{m\,s^{-1}}$.

2.3 Temporal autocorrelation function

Temporal autocorrelation measures the relationship between a signal in a time series and delayed versions of itself across different time lags. Figure 3 shows the autocorrelation function of the SPB measurements (black solid curve), where the time lag (t_l) is normalized by the autocorrelation time (t_a), $\tau = t_\mathrm{l}/t_\mathrm{a}$. The dashed curve shows the normalized autocorrelation from perfectly band-limited white noise (frequency spectrum cut off exactly at N), $\mathrm{sinc}(\tau) = \sin(\pi\tau)/(\pi\tau)$, evaluated with $t_\mathrm{a} = t_\mathrm{b}/2 = \pi/N$, with zero crossings at multiple integers of t_a (*i.e.*, $\tau = 1, 2, \cdots$). The correlation in the SPB data set falls

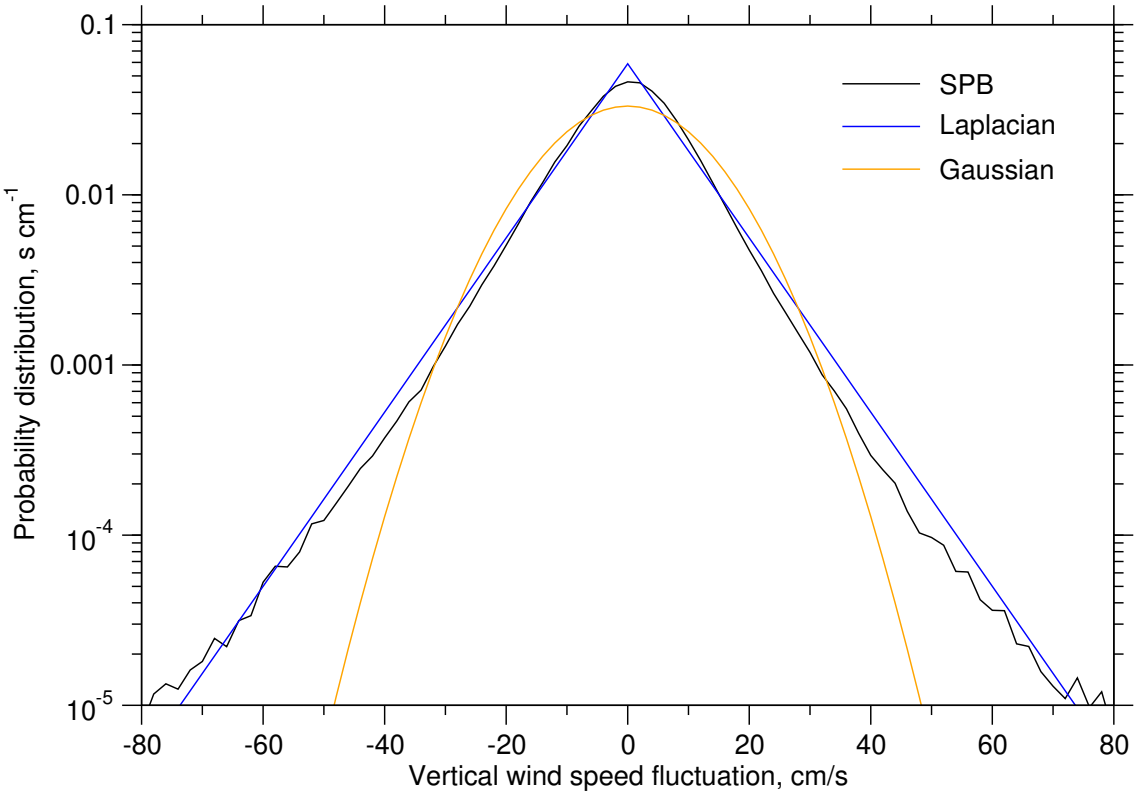

Figure 2. Probability distribution of vertical wind speed fluctuations from (solid curve) long-duration SPB observations in the TTL. A (blue) double-sided exponential and (orange) normal distribution evaluated with zero mean and the same standard deviation are shown for comparison.

off steeply reaching zero at 2 followed by a weak secondary peak at 3. This comparison suggests that the damped periodic sequence in the autocorrelation function of the SPB measurements may result from low pass filtering at N (section 2.1.1).

For comparison, Fig. 3 additionally shows an exponential autocorrelation function, $\exp(-\tau)$. The underlying stochastic model assumes an autoregressive process in line with Podglajen et al. (2016). The triangular function assumes back-to-back
105 rectangular signals with a fixed width of unity and randomly fluctuating magnitudes with zero mean, *i.e.*, the underlying time series consists of alternating boxcars each t_a long (Kärcher and Podglajen, 2019). The associated autocorrelation function is given by a triangle with base length of 2: $(1-\tau)$ for $|\tau| \leq 1$ and zero for $|\tau| > 1$. The corresponding synthetic time series derived from the triangular and exponential models (section 4) will be used alongside the SPB data to generate probability distributions of nucleated ice crystal number concentrations.

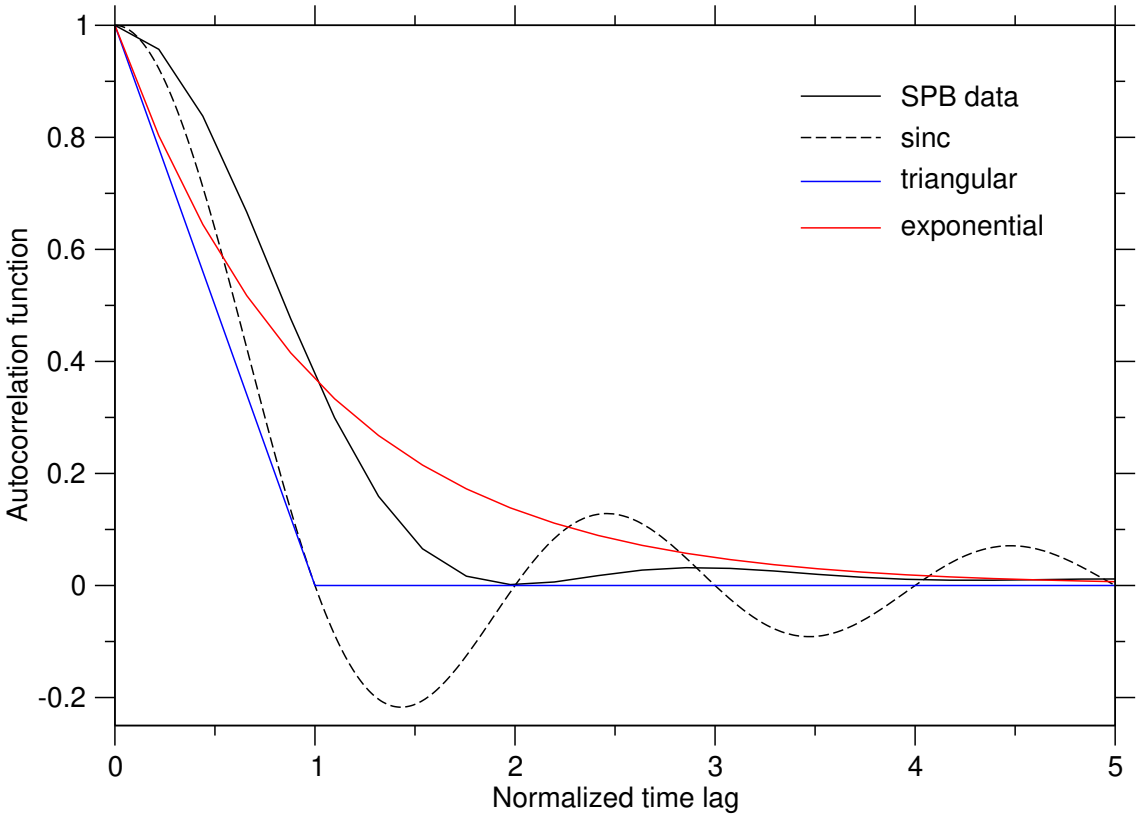

Figure 3. Autocorrelation vs. dimensionless time lag of N-filtered vertical wind speed fluctuations from (black curve) long-duration SPB observations in the TTL. A (blue) triangular and (red) an exponential model for the autocorrelation function are shown for comparison together with a (dashed) sinc function. The time lag is normalized by the autocorrelation time. Note that the left half of the triangle appears when extending the graph to negative time lags.

2.4 Power spectral density

The power spectral density (PSD) of the time series of a stochastic process measures how the fluctuation power is distributed in the frequency domain and is equal to the Fourier transform of its autocorrelation function (Gardiner, 1985, Ch. 1.4.2). Power spectra were obtained by applying a Fast Fourier Transform (FFT) to the discrete SPB and the synthetic time series data (Press et al., 1992, Ch. 12.2). The temporal resolution of the measurements is used in all cases, corresponding to a Nyqvist frequency of $1.67 \times 10^{-2}\,\mathrm{Hz}$ that lies well above $N/(2\pi)$. For computational efficiency, the full time series was divided into $1{,}356$ overlapping data blocks of length 2^{10}. The small block length yields a frequency resolution still fine enough to study high frequency features in the PSD, but compromises the detection of frequencies lower than about $10^{-4}\,\mathrm{Hz}$. The FFT was applied separately to each block after running a Hann window to reduce spectral leakages and the resulting one-sided power spectra were averaged to minimize statistical noise.

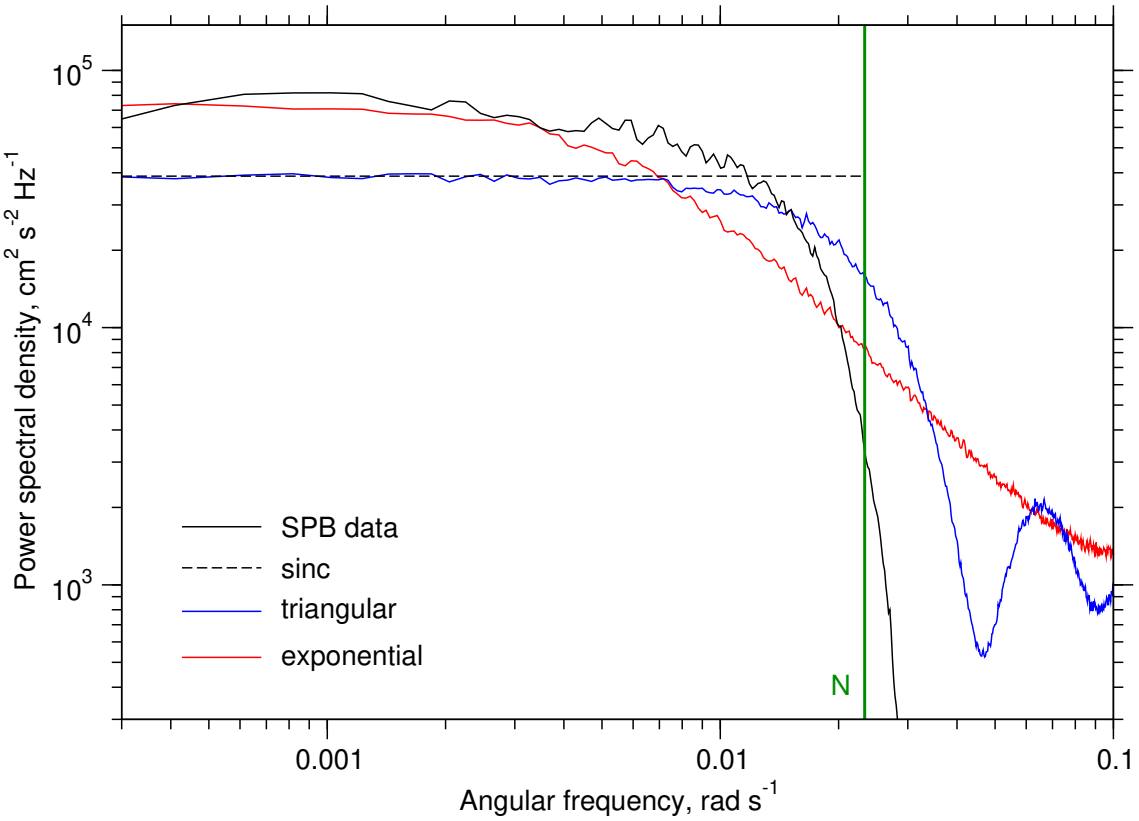

Figure 4. Power spectral densities of vertical wind speed fluctuations vs. angular frequency from (black) long-duration SPB observations in the TTL and (blue, red) synthetic time series consistent with the autocorrelation functions shown in Fig. 3. The total power contained in each case is close to σ_w^2. The average value of the buoyancy frequency, N, is indicated by the green vertical line. The analytical PSD from perfectly band-limited white noise, cut off at N and corresponding to a sinc-autocorrelation, is shown for comparison.

The PSD of vertical wind speed fluctuations due to GWs, S_w, from the N-filtered balloon data is given in Fig. 4. The effect of filtering on the distribution are shown in Jensen et al. (2026, Fig. 1). The low pass filter applied around N (section 2.1) causes the SPB power spectrum to decrease rapidly before, and roll off across, N, deviating from the idealized top hat distribution that extends only up to N. In nature, the propagation of wave packets, representing non-stationary bursts of GW activity, can cause an increase of power near N (Podglajen et al., 2016, Supporting Information, Text S1). Clearly, the N-filtered data set can no longer provide evidence for such intermittency features in the PSD.

In addition, PSDs are shown from two numerically generated time series whose autocorrelation functions are also presented in Fig. 3. The blue curve is consistent with triangular autocorrelation and is given by a cardinal sine function, whose first side lobe is visible. An exact solution would yield zero power at frequencies that are even multiples of N. The FFT cannot fully reproduce these zero crossings because of the smoothing action of the applied Hann window and because the frequencies employed do not exactly coincide with $2N, 4N, \cdots$. The red curve is consistent with the exponential correlation function and is

given by a Lorentzian that rolls off much more gradually across N than the SPB spectrum indicates (section 4.4). Because the true power spectrum and autocorrelation function of vertical wind speed fluctuations at high frequencies are not known due to the filtering, an N-filtered white noise source (dashed curve) is not necessarily more realistic and will therefore no longer be considered in this study.

3 Microphysical simulation model

3.1 Salient features

The DICE code (Dynamically-forced ICe nucleation and non-Equilibrium growth) is a versatile tool simulating homogeneous ice nucleation via solution droplet freezing; heterogeneous ice nucleation from time-dependent immersion freezing and time-independent deposition nucleation or pore condensation and freezing; and non-equilibrium droplet and ice crystal growth by uptake of water vapor. The treatment of ice crystal aggregation is optional. The numerical parcel model is based on conservation laws governing the temporal evolution of gaseous, liquid, and solid water phases in air adiabatic parcels accounting for water phase transitions induced by ice nucleation and deposition growth. The code efficiently solves a large set of coupled differential equations governing the temporal evolution of air pressure, absolute temperature, water vapor mass mixing ratio, and size-dependent particulate (liquid and frozen) water and associated aerosol core particle number and mass mixing ratios.

3.2 Model equations

The DICE code simulates aerosol and ice microphysical processes (aerosol-ice interactions) in a closed Lagrangian air parcel. Liquid solution droplets are defined as two separate particle populations with predefined number-size distributions: a background aerosol with dry, fully soluble cores that are not ice-active and a similar population with insoluble cores immersed in the solution that act as freezing nuclei. These two aerosol types may differ in physical properties, chemical composition, and water condensation efficiency (Kärcher and Koop, 2005). Hygroscopic droplet growth and homogeneous (and immersion) freezing of supercooled liquid water is calculated based on the simulated, non-equilibrium water activity of the solution. A number of aerosol particles can also form ice crystals according to deterministic activation spectra, analogous to traditional condensation nuclei activation.

While solution droplets grow to their exact sizes, ice deposition growth is simulated across a fixed size structure with geometrically progressive bins (fixed bin volume ratio) and variable bin centers. Growth of ice crystals by surface kinetics-limited diffusional water vapor uptake employs either variable deposition coefficients from an ice supersaturation- and size-dependent uptake parameterization or constant values (Kärcher et al., 2023). Ice crystals either pre-existing or nucleating from each aerosol type are lumped together into one ice cloud category.

The vertical wind speeds are given by the rapidly fluctuating components due to mesoscale waves, directly driving the rate of change of air temperature via adiabatic cooling or heating due to the short time scales involved (Eq. 16). As DICE is used for cirrus simulations at low temperatures ($< 230\,\mathrm{K}$), the transfer of heat between the water phases is not accounted for due to

its small contribution to the temperature tendency. Changes in air pressure are caused by adiabatic compression and expansion. The air mass density follows from the ideal gas law for dry air as the contribution from water vapor is negligible.

Along with these thermodynamic equations, DICE solves differential equations governing the evolution of total water mass during liquid and ice particle growth and ice nucleation (subscript nuc). Water vapor (subscript v) is transferred towards and away from water-containing particles by condensation or evaporation ($\mathrm{con/evap}$) and deposition or sublimation ($\mathrm{dep/subl}$) based on size-dependent particle mass mixing ratios, q, and particle number mixing ratios, η. Both variables are not affected by adiabatic (vertical) motion. Core particles (c) in liquid droplets include soluble (sol) matter or insoluble immersion nuclei.

Mass and number mixing ratios for particulate components with single particle volumes, V, and bulk mass densities, ρ, are related by $q = \rho V \eta$. Sizes of aqueous particles (subscript w) and ice crystals (i) are derived from their respective single particle volumes and are interpreted as radii, r, of volume-equivalent spheres. While different types of aerosol and core particles are described by their own set of number and mass mixing ratios, ice crystals nucleated from all of them are not tracked separately, but are described by a single set of mixing ratios.

Solution droplet growth is simulated employing a parameterization based on laboratory measurements and Köhler theory (Petters and Kreidenweis, 2007), wherein the water activity (a_w) is given by

$$a_w = \frac{V_w}{V_w + \kappa V_{\mathrm{sol}}}\,. \tag{2}$$

The hygroscopicity parameter $0 \leq \kappa \leq 1$ allows the calculation of kinetic mass growth rates of both, non-activated aqueous haze particles ($a_w < 1$) and cloud water droplets ($a_w \to 1$). For both, liquid droplets and ice crystals, the rate of water vapor transfer ($\mathcal{Z}$) by diffusion from the gas phase to particles (Lamb and Verlinde, 2011) can be cast into the form

$$\mathcal{Z} = 4\pi\beta D_v n\, r\,, \quad \beta = \Big(\frac{r}{r+\lambda} + \frac{\ell}{\alpha r}\Big)^{-1}, \tag{3}$$

where D_v is the diffusion coefficient of water molecules in air, ℓ is their diffusion length scale, and n is the number concentration of particles with radius r. The factor β corrects for surface attachment effects (Zhang and Harrington, 2014) that become important for particles with sizes similar to the mean free path (λ) of water molecules in air and α denotes the condensation/evaporation coefficient for liquid droplets or the particle-average deposition/sublimation coefficient for ice crystals.

The rates of change of condensate mass mixing ratios due to water phase transitions are given by

$$\frac{dq_w}{dt} = \frac{dq_w}{dt}\Big|_{\mathrm{con/evap}} + \frac{dq_w}{dt}\Big|_{\mathrm{nuc}}, \tag{4}$$

$$\frac{dq_i}{dt} = \frac{dq_i}{dt}\Big|_{\mathrm{dep/subl}} + \frac{dq_i}{dt}\Big|_{\mathrm{nuc}}, \tag{5}$$

together with the underlying diffusional growth laws

$$\frac{dq_w}{dt}\Big|_{\mathrm{con/evap}} = \mathcal{Z}_w(q_v - a_w K_w e_w)\,, \tag{6}$$

$$\frac{dq_i}{dt}\Big|_{\mathrm{dep/subl}} = \mathcal{Z}_i(q_v - K_i e_i)\,, \tag{7}$$

with the water vapor mass mixing ratios of supercooled water/hexagonal ice in thermodynamic equilibrium, $e_{w/i}$ (Murphy and Koop, 2005), and the Kelvin (curvature) corrections, $K_{w/i}$. For liquid particles, $K_w = \exp(A_w/r_w)$ with $A_w = 1\,\mathrm{nm}$ consistent with the water activity-based solubility model. For ice crystals, $K_i = \exp(A_i/r_i)$ with $A_i = 2\,\mathrm{nm}$ is sufficiently accurate.

This system of equations is closed by the conservation of total water, expressed in terms

$$\frac{dq_v}{dt} = -\Big(\sum_{r_w} \frac{dq_w}{dt}\Big|_{\mathrm{con/evap}} + \sum_{r_i} \frac{dq_i}{dt}\Big|_{\mathrm{dep/subl}}\Big)\,, \tag{8}$$

where the sums run over all respective particle size categories.

The numerical solvers for these microphysical processes are non-iterative, exactly mass-conserving, and unconditionally stable (Jacobson, 2005) and simulate the condensation/evaporation rates and water activity in the solution droplets as well as the deposition growth/sublimation rates of ice crystals. While droplets and their cores are tracked without reference to a size grid allowing them grow or shrink to their exact radii, ice crystal growth and sublimation is treated using a grid with geometrically progressing bin volumes and moving bin centers. The latter basically eliminates numerical diffusion in the air parcel framework.

Ice nucleation in water particles changes the associated liquid water and ice mass mixing ratios according to

$$\frac{dq_i}{dt}\Big|_{\mathrm{nuc}} = -\frac{dq_w}{dt}\Big|_{\mathrm{nuc}} = j_{\mathrm{hom}}\, q_w\,, \tag{9}$$

where $j_{\mathrm{hom}} = V_w J(a_w, T)$ is the homogeneous freezing rate based on the rate coefficient, J (Koop et al., 2000). Core material in liquid droplets is also transferred to ice crystals during droplet freezing; the resulting core mass mixing ratios follow from

$$\frac{dq_{i,c}}{dt}\Big|_{\mathrm{nuc}} = -\frac{dq_{w,c}}{dt}\Big|_{\mathrm{nuc}} = j_{\mathrm{hom}}\, q_{w,c}\,. \tag{10}$$

The second liquid aerosol population can undergo immersion freezing in a similar manner based on separate liquid water mass and number mixing ratios and immersion freezing rate. Several ice nucleation models are implemented to represent immersion freezing. Similar equations hold for the time tendencies of number mixing ratios of both, the two liquid aerosol types and their core material. Dry aerosol particles that nucleate ice heterogeneously do not interact with water vapor, but are otherwise described by rate equations similar to Eqs. 5, 7, and 10. Associated deterministic ice activation spectra result from integrating the product of ice-supersaturation- and size-dependent ice-active fractions and number-size distributions over particle size, replacing Eq. 9 (Kärcher and Marcolli, 2021, Eq. 14).

The TTL nucleation simulations are forced by vertical wind speeds from SPB time series (section 2.1) and three stochastic models representing the GW-induced fluctuations (section 4). Vertical air motion variability from these forcings causes fluctuations in temperature (section 4.4) that drive the microphysical processes *via* changes in ice supersaturation. The simulations are initialized close to the tropical tropopause where the balloon data were taken, at a pressure of $100\,\mathrm{hPa}$ and temperature of $192\,\mathrm{K}$. This study considers homogeneous freezing from background liquid aerosol particles. Each simulation starts with a log-normal number-size distribution (total droplet number concentration of $500\,\mathrm{cm}^{-3}$, dry modal radius of $20\,\mathrm{nm}$, geometric standard deviation of 1.5), and assumes a hygroscopicity parameter of 0.5. The initial supercooled liquid water content is

determined assuming thermodynamic equilibrium with environmental air. For aqueous droplets, the condensation coefficient is set to unity. For ice crystals, a deposition coefficient of 0.7 is used (Skrotzki et al., 2013), because HFEs evolve at high ice supersaturation.

3.3 Implementation of the gravity wave forcing

The DICE code is employed in an ensemble mode to generate probability distributions of nucleated ice crystal number concentrations. In this way, DICE simulates a large number of individual HFEs both from the measured and three synthetic time series using a time step of $0.1\,\mathrm{s}$. For each ensemble, DICE is called $80{,}000$ times with different fluctuation time series; about $50\,\%$ of them cool sufficiently on average, triggering freezing events and contributing to the ensemble statistics.

As the model time step is much smaller than the temporal resolution of the SPB data, the latter are linearly interpolated at the respective simulation times. While w'-fluctuations are computed online in the synthetic time series, each simulation in a given ensemble is initialized randomly along a different time of the full SPB time series. This ensures that each nucleation event is triggered by a unique sequence of statistically independent fluctuation amplitudes.

The stochastic WCPs predict exponentially or normally distributed w'-values online every time step (section 4). To generate random numbers and sample probability distribution functions, DICE employs the portable software packages RANLIB (Ahrens and Dieter, 1972) and RNGLIB (L'Ecuyer and Cote, 1991).

3.4 Numerical representation of low concentration homogeneous freezing events

To minimize computer time, carrying out tens of thousands of successive simulations requires stopping individual simulations as soon as no further ice crystals can form. While stopping the simulations is straightforward when using a constant updraft speed, the presence of random up- and downdrafts due to GW forcing requires some consideration.

All simulations in a given ensemble start at an ice saturation ratio of $S_i = 1.57$, right before homogeneous freezing commences. The onset threshold for homogeneous solution droplet freezing at $192\,\mathrm{K}$ is $S_\mathrm{i} \approx 1.6$. Cloud chamber measurements suggest a higher threshold at such low temperatures (Schneider et al., 2021). This finding is not accounted for, because the experimental study did not finally conclude on the observed difference in freezing onsets. Correcting for this difference would imply adjusting the parameterization of the saturation vapor pressure for supercooled liquid water at temperatures below $205\,\mathrm{K}$ (Nachbar et al., 2019) in the simulation of water activity in the droplets.

The simulations assume an HFE to be completed when deposition growth of the freshly nucleated ice crystals drives S_i more than a given amount, δS_i, below the initial value. The time for S_i to decrease can become very long in slow updrafts and thus low nucleated number concentrations. Due to the random forcing, a strong updraft may occur in the slowly declining supersaturation, adding copious new ice crystals. In such cases, the original low concentration HFE is counted as a higher concentration event. This results in an underestimation of low nucleated number concentrations in the distribution. Just how much a low number concentration HFE is affected by this mechanism depends on the choice of δS_i. More such events are counted the smaller δS_i is chosen. In DICE, δS_i is set to a value of 0.025.

This mechanism is not to be confused with quenching, where the vertical wind speed fluctuation changes sign during an HFE (Dinh et al., 2016). Quenching increases the number of low concentration events and is included in the present simulations. Generally, quenching becomes less important at warmer temperatures due to faster supersaturation relaxation times and when the high frequency variability in the GW forcing is reduced; see Jensen et al. (2026, Figs. 13+14) for a detailed analysis of quenching in TTL cirrus formation.

4 Wave-cirrus parameterizations

This section introduces several stochastic models that represent high frequency variability in vertical wind speeds due to GWs. The models are uniqely defined by their stationary statistics, *i.e.*, the probability distribution of the fluctuations, and the power spectrum (alternatively, the temporal autocorrelation function). All WCPs are fully constrained by just two parameters with clear physical meaning: first-order autocorrelation time, t_a, and total fluctuation power, σ_w^2.

4.1 Laplacian fluctuations with triangular autocorrelation

Kärcher and Podglajen (2019, hereinafter referred to as KP19) developed a stochastic model that directly incorporates the observed Laplacian statistic of w'. This approach describes a GW-related noise process that behaves like white noise over long time scales, but is fully correlated over short time scales. This means that the fluctuations have a finite memory.

A random fluctuation, $w'_k \equiv w'(t_k)$, of either sign is drawn from the Laplacian probability density (Eq. 1) at times $t_k = kt_\mathrm{a}$ ($k = 0, 1, 2, \cdots$) *via*

$$w'_k = -\mathrm{sgn}(\eta - 0.5) \cdot b\zeta\,, \tag{11}$$

and is kept constant up to t_{k+1}, where a new fluctuation, differing in magnitude and perhaps sign, is drawn. In Eq. 11, $\mathrm{sgn}(x) = \pm 1$ maps the value of $x \neq 0$ to its sign, $\eta \in [0, 1]$ is a uniformly distributed, random deviate, and ζ is a random deviate drawn every autocorrelation time from a standard exponential distribution.

The fluctuations are fully correlated at time scales shorter than the time increment t_a and totally uncorrelated at longer time scales, hence, short-term refers to correlations on the order of minutes, keeping high frequency variability in the fluctuation time series consistent with the SPB measurements.

The randomly alternating boxcar time series of the KP19 scheme with its triangular autocorrelation function (Fig. 3) has the PSD

$$S_w(f) = \sigma_w^2 t_\mathrm{a} \Big[\frac{\sin(\pi f t_\mathrm{a})}{\pi f t_\mathrm{a}}\Big]^2. \tag{12}$$

This PSD (Fig. 4) is approximately flat for frequencies $f \ll 1/t_\mathrm{a}$ ($S_w \to \sigma_w^2 t_\mathrm{a}$). In the high frequency limit $f \gg 1/t_\mathrm{a}$, the PSD develops side lobes with an envelope decaying as $1/f^2$. Because the amplitudes in the KP19 time series have sharp boundaries, the PSD extends beyond N.

4.2 Laplacian fluctuations with exponential autocorrelation

This model is also characterized by Laplacian distributed fluctuations (Farah and Lindner, 2021, hereinafter referred to as FL21), in line with the SPB measurements. Unlike KP19, the temporal autocorrelation function follows very closely an exponential decay. Given Δt as the time step of the microphysical model, random fluctuations w'_k of either sign follow at time stations $t_k = k\Delta t$ ($k = 1, 2, \cdots$) from the discretized stochastic differential equation

$$w'_k = w'_{k-1} - \mathrm{sgn}(w'_{k-1})\,\frac{5\tau_\mathrm{s}}{2}\,b + \sqrt{\frac{5\tau_\mathrm{s}}{2}}\cdot\sigma_w\,\xi\,, \tag{13}$$

where $\tau_\mathrm{s} = \Delta t/t_\mathrm{a}$ is the dimensionless time step and ξ is a random deviate drawn every time step from a normal distribution with zero mean and unit variance. The first fluctuation ($k = 0$) is sampled in each simulation from Eq. 11, and subsequent fluctuations decorrelate slowly over time. The $\sqrt{\Delta t}$-dependence is a hallmark of stochastic differential equations: when applied many times, the summed Wiener (Brownian motion) increments, $\sqrt{\Delta t}\,\xi$, approach Δt (Lemons, 2002, Ch. 6.2) in line with deterministic calculus. To obtain accurate solutions, Eq. 13 must be evaluated with $\tau \ll 1$.

The near-exponentially decaying correlation (Farah and Lindner, 2021, Fig. 1d), here shown in Fig. 3, is approximately consistent with the Lorentzian PSD (Fig. 4),

$$S_w(f) = \frac{1}{\pi}\,\frac{\sigma_w^2 t_\mathrm{a}}{1 + (f t_\mathrm{a})^2}\,. \tag{14}$$

Similar to the KP19 spectrum and with t_a from section 2.1, $S_w \propto f^{-2}$, is realized for frequencies $f \gg N/\pi$. Conversely, for $f \ll N/\pi$, the spectrum is approximately flat ($S_w \to \sigma_w^2/N$).

4.3 Gaussian fluctuations with exponential autocorrelation

Owing to the central limit theorem, applications using normally distributed variables are very widespread across science and engineering. It is therefore instructive to explore how the use of a Gaussian model for w' compares with results from the above Laplacian schemes, although the latter yield a better approximation of the observed fluctuation distribution (Fig. 2). The Ornstein-Uhlenbeck stochastic process (Uhlenbeck and Ornstein, 1930, hereinafter referred to as OU30) is characterized by an exponential autocorrelation function and, contrary to KP19 and FL21, by normally distributed fluctuations.

While fluctuations from OU30 can be derived from a stochastic differential equation (Lemons, 2002, Ch. 7), the algorithm employed here (Bartosch, 2001) is independent of the time step. Random fluctuations w'_k of either sign follow at time t_k ($k = 1, 2, \cdots$) from the stochastic evolution equation,

$$w'_k = C_k\,w'_{k-1} + \sqrt{1 - C_k^2}\cdot\sigma_w\,\xi \tag{15}$$

where $C_k = \exp(-|t_k - t_{k-1}|/t_\mathrm{a})$ is the autocorrelation between successive time stations. The first fluctuation ($k = 0$) is sampled from a Gaussian, $w'_0 = \sigma_w\xi$. Equation 15 is exact for all values of C_k, *i.e.*, time steps. The power spectrum from this model is identical to Eq. 14.

Gaussian fluctuations can also be generated based on arbitrary power spectra. In the stochastic Fourier series expansion approach, sample paths of a stationary colored noise process are generated from an expansion in terms of harmonic functions according to the Spectral Representation Theorem (Shinozuka and Deodatis, 1991). This method leads to a Gaussian fluctuation statistic, similar to OU30. The advantage over OU30 is that the PSD can be chosen arbitrarily.

4.4 Notes on power spectra and temperature fluctuations

GW periods most relevant for TTL cirrus formation coincide with time scales of HFEs, typically $1\,\mathrm{min}$ for full nucleation events in the TTL (Jensen et al., 2016b, Fig. 4) penetrating the short period end of the GW forcing spectrum. Gravity waves cannot propagate at intrinsic frequencies above N (Fritts and Alexander, 2003), the range of microscale turbulence.

The power spectra of the SPB and the two synthetic Laplacian time series contain frequency components above N to various degrees (Fig. 4). With regard to the measurement data, a small amount of power is contained at intrinsic frequencies above N due to filtering. Another consequence of the filtering is the gradual decrease of power from about $N/2$ up to N, implying that the true fluctuation standard deviation may be larger than $12\,\mathrm{cm\,s^{-1}}$.

In the FL21 scheme, the PSD unfavorably extends much farther into the low and high frequency range (across N) than in the SPB case. The KP19 scheme exhibits a behavior that lies between that of SPB and FL21. In view of the unphysical nature (regarding GW propagation) of signals with intrinsic frequencies $\omega > N$ in the synthetic forcings, it will be interesting to see how sensitive the nucleation simulations respond to different degrees of high frequency variability (section 5). As noted in the introduction, differences in total power contained at low frequencies seen in Fig. 4 are not relevant for the simulation of HFEs.

Mesoscale temperature fluctuations (MTFs), T', arise from the action of GW-driven vertical wind speed perturbations. The fact that the autocorrelation time of w' fluctuations is not zero leads to a correlation between two successive air parcel displacements, hence, T'. White noise forcing $S_w(f) \propto f^0$ leads to red noise behavior of $S_T(f) \propto f^s$ with a spectral slope $s = -2$, implying that the majority of MTF variance is concentrated near the Coriolis frequency, ω_c, as the lowest possible intrinsic GW frequency. The associated vertical random walk of air parcels causes the ensemble-average MTF variance, σ_T^2, to increase over time, similar to a diffusive process.

Due to the short time scales involved, the vertical wind speed fluctuations drive the rate of change of air temperature via adiabatic cooling or heating,

$$\frac{dT'}{dt} = -\Gamma w' - \lambda T' \,, \tag{16}$$

with the dry adiabatic lapse rate, Γ. With Eq. 16, the KP19 scheme accounts for a low frequency damping of the MTFs at a rate $\lambda = \mathcal{O}(\omega_\mathrm{c})$ to prevent σ_T from reaching values larger than $\Gamma\sigma_w/\sqrt{\omega_\mathrm{c} N}$ (Kärcher and Podglajen, 2019, Eq. 11). The first-order autoregressive model proposed by Podglajen et al. (2016, Supporting Information, Text S2) for MTF is largely equivalent to KP19, but assumes $\lambda = 0$ and thus leaves the MTF variance asymptotically unconstrained. The slow (several hours) MTF damping is not considered in the WCPs, which focusses on predominantly short (several minutes) nucleation events. Recall from Sect. 2.1 that the SPB data are already filtered to eliminate periods longer than 1 day.

Negative spectral slopes in S_T imply smaller susceptibility of T' to intermittent perturbations than w'. In fact, measured T'-values associated with GW activity are typically normally distributed in the tropics and over high-latitude oceanic regions (Gary, 2006; Podglajen et al., 2016). It turns out that such background conditions are met sufficiently far away from source regions of convective GWs, *e.g.*, in the TTL at distances greater than $200\,\mathrm{km}$ away from lower level convective activity (Corcos et al., 2021). Applying KP19 or FL21 to simulate HFEs based on w'-data as in the present study is justified in such conditions.

Intermittency in GW activity may cause exponential tails also in the temperature distributions (Bacmeister et al., 1999; Podglajen et al., 2016) or may be identfied as spectral features in, or deviations from an average spectral slope of, power spectra. Intermittency may be caused by flow over mountains, and to a lesser degree by convection. The FL21 scheme can be used to model exponentially distributed MTF along with an $s \approx -2$ scaling of the associated power spectrum at high frequencies, circumventing the use of vertical wind speed fluctuations. The Fourier series approach can be applied to model MTFs closer to their source region, where the frequency scaling of S_T may deviate from an $s = -2$ power law, but with normally distributed MTFs. It is not immediately obvious how to model exponentially distributed MTFs with arbitrary noise color. It is therefore not immediately obvious how to quantify the effect of frequency composition changes in GW spectra on TTL cirrus formation close to convective source regions (Corcos et al., 2021, Fig. 10).

5 Ice nucleation simulations

Homogeneous freezing events are very sensitive to vertical wind speed fluctuations, *i.e.,* cooling and heating rates. This section discusses probability distributions of homogeneously nucleated ice crystal number concentrations, $dP/d\log_{10}(n)$, in the TTL. Three WCPs are employed and the probability distributions simulated with them are compared to the statistic directly simulated with the SPB forcing. They are constrained by $t_\mathrm{a} = 2.25\,\mathrm{min}$ and $\sigma_w = 12\,\mathrm{cm\,s^{-1}}$ inferred from the filtered SPB data, making the simulated statistics from all forcings directly comparable.

5.1 SPB forcing

Out of $80{,}000$ calls per ensemble, about one half of the w'-trajectories start with a prolonged warming period and thus do not readily lead to ice nucleation. These cases are excluded from the statistics. Figure 5 shows the probability density along with its cumulant from one ensemble, based on 39,038 simulation data points associated with a fully developed or quenched homogeneous freezing event. Statistics of homogeneously nucleated ice numbers are broad, very high concentrations are occasionally possible, and the low number concentration tail is affected by quenching (Jensen et al., 2026, Sect. 3). The latter means the premature termination of a nucleation event due to a sudden warming fluctuation, decreasing n relative to an unquenched event. The accurate prediction of low concentration HFEs in the ice probability statistic is not without challenge, as this depends on how the duration of HFEs is defined in the simulations (section 3.4).

Due to the large number of low updraft speeds in the GW forcing, the median concentration is much smaller than the mean value; $50\,\%$ of HFEs lead to ice crystal number concentrations up to $0.4\,\mathrm{cm^{-3}}$. As the frequency of occurrence of high updraft

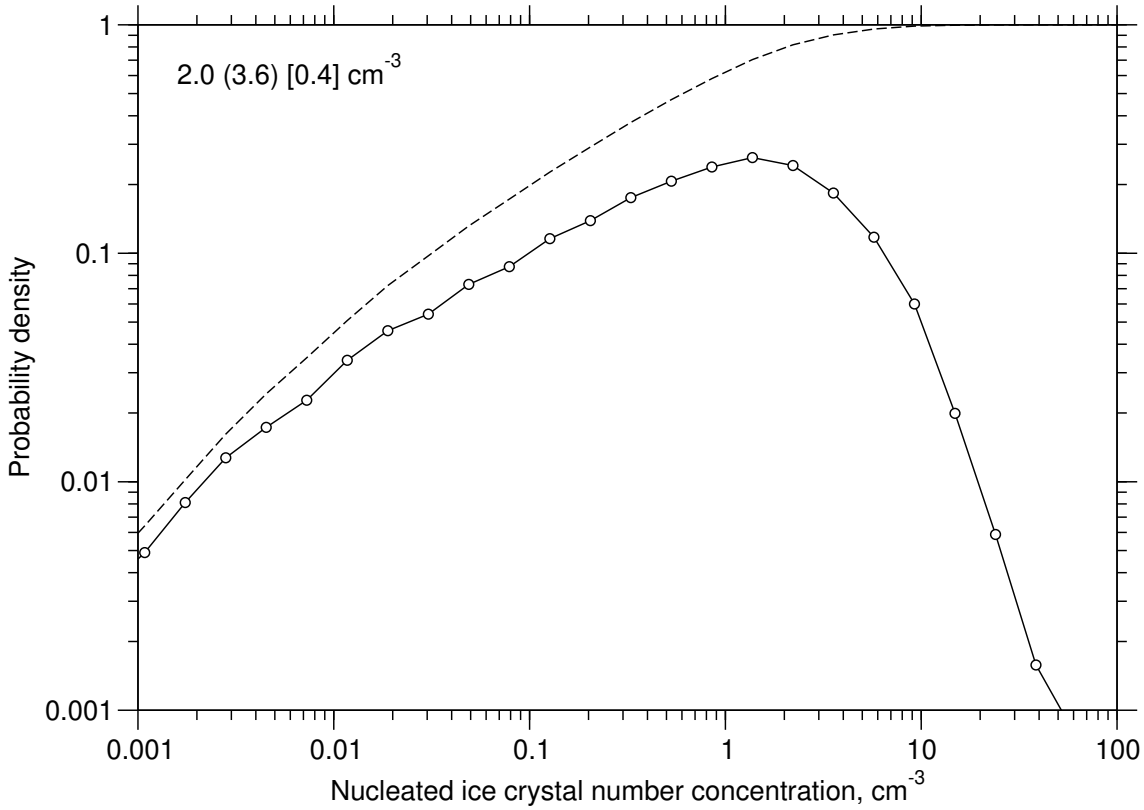

Figure 5. Probability distribution of homogeneously nucleated ice crystal number concentrations from TTL simulations forced by the N-filtered SPB measurements. The dashed curve shows the associated cumulative distribution. The legend provides the mean (standard deviation) [median] concentration.

speeds decreases exponentially, the ice distribution falls off steeply at high concentrations. The cumulative distribution shows that about 1 % of all data points lead to $n > 10\,\mathrm{cm}^{-3}$; one HFE produced $144\,\mathrm{cm}^{-3}$ ice crystals and is off the scale in Fig. 5.

TTL cirrus occur preferentially in negative temperature anomalies due to planetary and equatorial waves (Kim et al., 2016; Podglajen et al., 2018). Therefore, adding a slow vertical wind speed to the GW forcing in the simulations mimicks the presence of a low frequency wave. As a consequence, frequencies of occurrence of the smallest updraft speeds are expected to decrease, removing part of the distribution at low concentrations. Separate simulations (not shown) indicate that adding a constant updraft below $1\,\mathrm{cm\,s}^{-1}$ does not significantly alter the distribution in Fig. 5, leaving the median ice crystal number concentration basically unaffected. This no longer holds for stronger updrafts.

5.2 WCP forcings

Figure 6 shows that the statistics derived from the two Laplacian models (KP19 and FL21) compare well with each other, despite differences in autocorrelation and power spectra (section 2.1). The low concentration wings ($n < 0.1\,\mathrm{cm}^{-3}$) are in

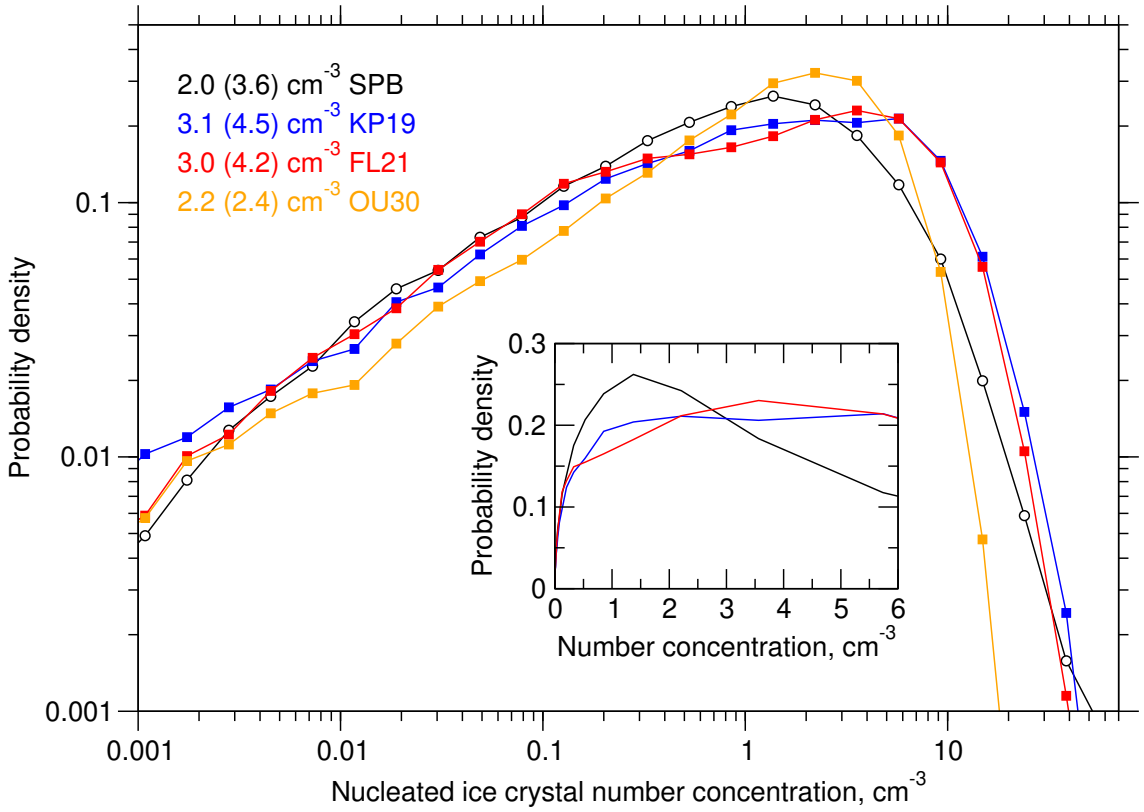

Figure 6. Probability distribution of homogeneously nucleated ice crystal number concentrations from TTL simulations forced by (blue) KP19, (red) FL21, and (orange) OU30. For comparison, the black distribution repeats the result directly simulated with the SPB forcing (Fig. 5). The legend lists the mean (standard deviation) concentration for each case. The inset repeats the distributions derived from SPB, KP19, and FL21 around the mean concentration on a linear scale.

good agreement with the statistic simulated directly with the SPB forcing. This suggests that the exact shape of the underlying power spectra at low frequencies (Fig. 4) is not a critical factor in ice nucleation simulations at low updrafts speeds. However, both WCPs predict more high concentration HFEs ($n > 2-3\,\mathrm{cm}^{-3}$) than the SPB forcing, causing the respective mean values to be larger. Updraft speeds exceeding σ_w are needed to generate such high concentrations.

Reducing σ_w in the WCPs does not correct this overestimation, as this would shift the entire nucleated ice number statistics to lower mean concentrations (Jensen et al., 2026, Fig. 10a) and thereby worsen the agreement at low concentrations. Increasing the autocorrelation times truncates high frequency variability in the WCP time series. For example, doubling t_a increases the probability of occurrence of updraft speeds around the peak region at the expense of higher updrafts (Jensen et al., 2026, Fig. 9b), which is confirmed here based on the KP19 or FL21 forcings (not shown). However, the value $t_\mathrm{a} = t_\mathrm{b}$ would decorrelate the synthetic fluctuations too slowly compared to the filtered SPB measurements (Fig. 3). Therefore, increasing t_a beyond $t_\mathrm{b}/2$ is dismissed as a potential corrective measure.

These results are in line with, but not identical to, those obtained using a different microphysical simulation model, the Community Aerosol and Radiation Model for Atmospheres (CARMA) bin microphysics model. While the KP19- and SPB-derived ice concentration distributions agree very well in CARMA simulations for $t_a = 3/N$ (Jensen et al., 2026, Fig. 8), a noticeable difference in the position of the distribution peak and the mean concentrations is found when using the nearly identical value $t_a = \pi/N$ in KP19 in DICE simulations (cp. blue and black curves in Fig. 2). Likely, the differences in the simulated ice number distributions are due mainly to intermodel spread, as both microphysical codes differ from each other in terms of model formulation and parameter settings, for example, regarding the thermodynamics and dry core volume of liquid solution droplets, the treatment of hygroscopic droplet growth, and the size gid over which particles grow.

The ice frequency statistic is also simulated with the OU30 approach that generates Gaussian w'-fluctuations. OU30 leads to fewer fluctuations above $30\,\mathrm{cm\,s^{-1}}$ than seen in the SPB data or obtained with the Laplacian WCPs (Fig. 2). Moreover, the use of OU30 consistenly underestimates low concentrations events with $n < 0.1{-}1\,\mathrm{cm^{-3}}$. The statistic simulated with OU30 is noticeably narrower, especially at high n, where ice concentrations $> 20\,\mathrm{cm^{-3}}$ are basically absent. It is therefore not included in the inset of Fig. 6. On the one hand, Laplacian vertical wind speed statistics in WCPs better capture extreme concentration HFEs. On the other hand, it is not known from aircraft measurements how often these extremely high ice concentrations occur, because such HFEs are rarely sampled due to their highly localized and transient nature.

6 Conclusions

6.1 Summary

The present study systematically evaluated the impacts of wave-cirrus parameterizations on homogeneous aerosol droplet freezing in TTL cirrus. To this end, time series of vertical wind speed fluctuations due to gravity waves from long-term, quasi-Lagrangian superpressure balloon measurements at the cold point tropical tropopause were analyzed. Fluctuation distribution, autocorrelation function, and power spectral density were generated and compared to those obtained from synthetic fluctuation time series derived from three stochastic wave-cirrus parameterizations. The latter are constrained by the autocorrelation time and total fluctuation power inferred from the measurement data and coupled to a microphysical simulation model. With the help of this model, probability distributions of homogeneously nucleated ice crystal number concentrations were computed and studied.

A direct juxtaposition of simulation results based on measured and parameterized data highlights that nucleated ice number concentrations statistics obtained from the schemes with exponentially distributed vertical wind speed fluctuations are in good overall agreement with that directly obtained from balloon-borne measurements filtered at the buoyancy frequency. A stochastic scheme with normally distributed fluctuations yields a narrower ice number distribution. Because of mixing and ice crystal settling, the statistics simulated with a parcel model may not reflect actual distributions in cirrus after the nucleation events occur. Intermodel differences in simulated probability distributions of ice concentrations are comparable to differences associated with properties of the size distribution of aerosol particles and the numerical treatment of processes affecting their

liquid water content. For given variance, the probability distribution of fluctuation amplitudes is as relevant for predicting ice concentrations as the power spectral behavior across the buoyancy frequency.

6.2 Discussion and implications

Dynamical variability in cirrus ice formation can rival that of aerosol-cirrus interactions. Despite the need to filter the balloon-borne vertical wind speed data in order to limit the impact of non-geophysical artifacts, these measurements are the best available experimental fingerprint of cloud-scale vertical air motion variability to date for direct use in Lagrangian parcel models of cirrus ice formation. It offers ample variability to statistically examine homogeneous freezing events. Simulating homogeneous freezing directly based on these data underestimates the homogeneously nucleated, mean ice crystal number concentration by $33\,\%$ compared to microphysical simulations based on constrained synthetic data. This difference manifests itself in the smaller number of freezing events with ice concentrations in the range $3-40\,\mathrm{cm}^{-3}$ in the measurement-based statistic compared to the model statistics, which instead appear as a surplus of events with concentrations in the range $0.2-3\,\mathrm{cm}^{-3}$ (Fig. 6). While differences in power spectra near the buoyancy frequency between the measurements and models (Fig. 4) likely contribute to this discrepancy, we hypothesize that the necessary filtering of the measurement data is the main cause of the underestimation.

The floating balloon measurements provide fluctuations every $30\,\mathrm{s}$. The inset in Fig. 1 shows a short, randomly picked segment of the associated time series interpolated to the much smaller numerical model time step of $0.1\,\mathrm{s}$. The synthetic time series provide new fluctuations every time step. Due to the coarser temporal resolution of the measurement data, it is not known how fluctuations due to gravity waves evolve on the time step level. At any rate, the filtering smoothens consecutive w'-data preferentially at high frequencies. The associated lack of fast cooling rates appears as a redistribution of high to low concentration events.

Overall, KP19 might be favored over FL21 to represent gravity wave activity in cirrus models due to a better performance of its power spectrum across the buoyancy frequency and its straightforward implementation in cloud models. The KP19 scheme treats gravity wave activity in background conditions—exponentially distributed vertical wind speeds and normally distributed temperature fluctuations along with spectrally flat vertical wind speed and red noise temperature fluctuation power—for applications in cirrus microphysical studies in the tropical tropopause layer. The closer to the wave sources, the more intermittency causes fluctuation amplitudes to appear as localized, non-stationary wave packets. Intermittent gravity wave activity may manifest itself in fat tails in the fluctuation distributions, and by variations of the spectral slope or frequency-dependent features in the power spectra. It can be identified in greater detail through methods that go beyond the analysis of stationary time series. Dedicated approaches are needed to include such effects in wave-cirrus parameterizations.

The power contained in the vertical wind speed fluctuations near the buoyancy frequency can be enhanced by trapping of gravity waves near the tropopause, for which radar measurements in the tropics provide direct evidence (Kottayil et al., 2024). Trapping involves the formation of atmospheric ducts by thermal structures or the wind field and is more pronounced for internal GWs with short horizontal wavelengths, hence, high intrinsic frequencies (Fritts and Alexander, 2003). In situations where an enhancement of fluctuation power due to trapping occurs, the number concentration of homogeneously nucleated ice

crystals is expected to increase. Filtering of the balloon data necessary to remove vertical wind perturbations caused by non-geophysical oscillations also removes the potential impact of trapping on the total fluctuation power and spectral distribution. Even if the filtering of SPB data could be avoided, the role of wave trapping on cirrus formation, lifetimes, and coverage cannot be reliably assessed without a more complete understanding of the power and spectral composition of the associated wind speed perturbations.

Beyond the buoyancy frequency, vertical air motion variability may be associated with irreversible turbulent mixing at times scales < 1 min and vertical scales < 100 m. Data filtering also removes the potential impact of turbulence. Turbulence intensity can vary widely at cirrus altitudes (Atlas and Bretherton, 2022) and the associated vertical motions can have a marked impact on homogeneous freezing events in their own right (Kärcher et al., 2025, Fig. 5). Research is still nascent on the effects of microscale turbulence for ice nucleation in cirrus. In particular, effects of wave-turbulence coupling on cirrus formation remain to be explored, as breaking of gravity waves is a key source of turbulence.

Balloon observations of gravity wave activity are not available in the midlatitude upper troposphere, where wave sources are mainly related to orography, unstable shear layers, and weather perturbances. In the absence of direct experimental information, a step towards learning more about the impact of gravity waves on the lifecycles of natural cirrus and contrail cirrus clouds in this region (Kärcher and Corcos, 2025) would be to analyze how much wave-induced variability in updraft speeds is simulated with high resolution global models (Noble et al., 2026) and needs no longer be parameterized.

Lagrangian parcel models may be used to validate parameterizations of ice nucleation in cirrus that are driven by parameterized cloud-scale updraft fluctuations in global models (Lyu et al., 2025). Most global climate models drive ice nucleation parameterizations with tuned turbulence kinetic energy (Lohmann and Kärcher, 2002). While this approach may get the mean nucleated concentrations right, intermittency effects are not accounted for, associated statistics of ice number concentrations are too narrow, and temporal and spatial patterns of cirrus occurrence may not be correctly represented. In the case of orographic gravity waves, this led to a lack of a representation of lee wave cirrus in global model simulations (Dean et al., 2005).

The wave-cirrus parameterizations investigated here are intermediate solutions aiming at improving the model representation of cirrus in process-based and global models. They do not account for specific wave sources, because they describe universal background conditions. In particular, they do not cover intrinsic frequency composition changes depending on the distance to wave sources and effects of wave trapping. Ideally, ice nucleation schemes in global models rely on wave-cirrus parameterizations that are fully interactive with the model's resolved atmospheric state and faithfully reproduce associated spatially and temporally variable properties of gravity waves from all sources.

Code and data availability. The Stratéole-2 campaign was sponsored by CNES, CNRS/INSU, and NSF and the measurement data set is available from https://doi.org/10.14768/7396b9ec-582f-4be2-8c37-c34ef41247a7 (version v3b). The model data sets generated for this study are hosted by Zenodo, https://doi.org/10.5281/zenodo.22662438. The model source code is not publicly available.

Author contributions. B. K. designed the study, carried out the simulations, and wrote the manuscript.

Competing interests. The contact author declares that there are no competing interests.

Acknowledgements. I thank Milena Corcos, Eric Jensen, and Hugh Morrison for helpful suggestions and valuable comments on the manuscript. This work has been facilitated by the Forstenried Laboratory for Cloud Physics (FoCP).

Table 1. Acronyms

CARMA	community aerosol and radiation model for atmospheres (microphysics model)
DICE	dynamically-forced ice nucleation and non-equilibrium growth
FFT	fast Fourier transform
GW	internal gravity wave
HFE	homogeneous freezing event
MTF	mesoscale temperature fluctuation
PSD	power spectral density
SPB	superpressure balloon
TTL	tropical tropopause layer
WCP	wave-cirrus parameterization

Table 2. Mathematical symbols in the main text

Symbol	Meaning	SI-Unit
b	scale parameter of Laplacian distribution ($\sigma_w/\sqrt{2}$)	$\mathrm{m\,s^{-1}}$
C	autocorrelation function (normalized autocovariance)	$-$
Δt	timestep of microphysical model	s
f	frequency	Hz
Γ	absolute value of the dry adiabatic lapse rate	$\mathrm{K\,m^{-1}}$
λ	low-frequency damping rate of mesoscale temperature fluctuations	$\mathrm{s^{-1}}$
n	nucleated ice crystal number concentration	$\mathrm{m^{-3}}$
N	Brunt-Väisälä (buoyancy) frequency	$\mathrm{rad\,s^{-1}}$
η	random deviate drawn over [0,1] from uniform distribution	$-$
P	probability	$-$
s	slope of power spectrum	$-$
S_i	ice saturation ratio	$-$
S_x	power spectral density of variable x	$\mathrm{dim}[x^2]\,\mathrm{Hz^{-1}}$
σ_x	standard deviation of variable x	$\mathrm{dim}[x]$
t	time	s
t_a	autocorrelation time	s
t_b	buoyancy period ($2\pi/N$)	s
t_l	time lag in autocorrelation function	s
T'	temperature fluctuation	K
τ	dimensionless time lag ($t_\mathrm{l}/t_\mathrm{a}$)	$-$
τ_s	dimensionless time step ($\Delta t/t_\mathrm{a}$)	$-$
w'	vertical wind speed fluctuation	$\mathrm{m\,s^{-1}}$
ω	angular frequency	$\mathrm{rad\,s^{-1}}$
ω_c	Coriolis (inertial) frequency	$\mathrm{rad\,s^{-1}}$
ξ	random deviate drawn from standard normal distribution	$-$
ζ	random deviate drawn from standard exponential distribution	$-$

References

Ahrens, J. and Dieter, U.: Computer methods for sampling from the exponential and normal distributions, Communications of the ACM, 15, 873–882, https://doi.org/10.1145/355604.361593, 1972.

Atlas, R. and Bretherton, C. S.: Aircraft observations of gravity wave activity and turbulence in the tropical tropopause layer: prevalence, influence on cirrus and comparison with global-storm resolving models, Atmos. Chem. Phys., 22, https://doi.org/0.5194/acp-23-4009-2023, 2022.

Bacmeister, J. T., Eckerman, S. D., Tsias, A., Carslaw, K. S., and Peter, T.: Mesoscale temperature fluctuations induced by a spectrum of gravity waves: A comparison of parameterizations and their impact on stratospheric microphysics, J. Atmos. Sci., 56, https://doi.org/10.1175/1520-0469(1999)056%3C1913:MTFIBA%3E2.0.CO;2, 1999.

Bartosch, L.: Generation of colored noise, Int. J. Mod. Phys. C, 12, https://doi.org/10.1142/S0129183101002012, 2001.

Corcos, M., Hertzog, A., Plougonven, R., and Podglajen, A.: Observation of gravity waves at the tropical tropopause using superpressure balloons, J. Geophys. Res., 126, https://doi.org/10.1029/2021JD035165, 2021.

Corcos, M., Hertzog, A., Plougonven, R., and Podglajen, A.: A simple model to assess the impact of gravity waves on ice crystal populations in the Tropical Tropopause Layer, Atmos. Chem. Phys., 23, https://doi.org/10.5194/acp-23-6923-2023, 2023.

Corcos, M., Kärcher, B., Lesigne, T., Podglajen, A., and Jensen, E.: On the role of atmospheric waves in governing the persistence of thin cirrus clouds in the Tropical Tropopause Layer [preprint], EGUsphere, 26, https://doi.org/10.5194/egusphere-2026-3112, 2026.

Dean, S. M., Lawrence, B. N., Grainger, R. G., and Heuff, D. N.: Orographic cloud in a GCM: the missing cirrus, Clim. Dyn., 24, https://doi.org/10.1007/s00382-005-0020-9, 2005.

Dean, S. M., Flowerdew, J., Lawrence, B. N., and Eckerman, S. D.: Parameterisation of orographic cloud dynamics in a GCM, Clim. Dyn., 28, https://doi.org/10.1007/s00382-006-0202-0, 2007.

Dinh, T., Podglajen, A., Hertzog, A., Legras, B., and Plougonven, R.: Effect of gravity wave temperature fluctuations on homogeneous ice nucleation in the tropical tropopause layer, Atmos. Chem. Phys., 16, https://doi.org/10.5194/acp-16-35-2016, 2016.

Farah, G. N. and Lindner, B.: Exponentially distributed noise—its correlation function and its effect on nonlinear dynamics, J. Phys. A: Math. Theor., 54, https://doi.org/10.1088/1751-8121/abd2fd, 2021.

Fritts, D. C. and Alexander, M. J.: Gravity wave dynamics and effects in the middle atmosphere, Rev. Geophys., 41, https://doi.org/10.1029/2001RG000106, 2003.

Gardiner, C. W.: Handbook of Stochastic Methods, Springer Verlag, Berlin, Heidelberg, New York, https://doi.org/10.1007/978-3-662-02452-2, 1985.

Gary, B.: Mesoscale temperature fluctuations in the stratosphere, Atmos. Chem. Phys., 6, https://doi.org/10.5194/acp-6-4577-2006, 2006.

Haase, J. S., Alexander, M. J., Hertzog, A., Kalnajs, L., Deshler, T., Davis, S. M., Plougonven, R., Cocquerez, P., and Venel, S.: Around the world in 84 days, EOS, 99, https://doi.org/10.1029/2018EO091907, 2018.

Hoyle, C. R., Luo, B. P., and Peter, T.: The origin of high ice crystal number densities in cirrus clouds, J. Atmos. Sci., 62, https://doi.org/10.1175/JAS3487.1, 2005.

Jacobson, M. Z.: Fundamentals of Atmospheric Modeling, Cambridge University Press, Cambridge, UK, 2nd edn., https://doi.org/10.1017/CBO9781139165389, 2005.

Jensen, E. J., Lawson, R. P., Bergman, J. W., Pfister, L., Bui, T. V., and Schmitt, C. G.: Physical processes controlling ice concentrations in synoptically forced, midlatitude cirrus, J. Geophys. Res., 118, https://doi.org/10.1002/jgrd.50421, 2013.

Jensen, E. J., R. Ueyama, L. P., Bui, T. V., Alexander, M. J., Podglajen, A., Hertzog, A., Woods, S., Lawson, R. P., Kim, J.-E., and Schoeberl, M. R.: High-frequency gravity waves and homogeneous ice nucleation in tropical tropopause layer cirrus, Geophys. Res. Lett., 43, https://doi.org/10.1002/2016GL069426, 2016a.

Jensen, E. J., Ueyama, R., Pfister, L., Bui, T. V., Lawson, R. P., Woods, S., Thornberry, T., Rollins, A. W., Diskin, G. S., Digangi, J. P., and Avery, M. A.: On the susceptibility of cold tropical cirrus to ice nuclei abundance, J. Atmos. Sci., 73, https://doi.org/10.1175/JAS-D-15-0274.1, 2016b.

Jensen, E. J., Corcos, M., and Kärcher, B.: Influence of variations in gravity wave properties on cirrus ice number concentrations produced by homogeneous freezing in the tropical tropopause layer, J. Geophys. Res., 131, https://doi.org/10.1029/2025JD044467, 2026.

Joos, H., Spichtinger, P., Lohmann, U., Gayet, J.-F., and Minikin, A.: Orographic cirrus in the global climate model ECHAM5, J. Geophys. Res., 113, https://doi.org/10.1029/2007JD009605, 2008.

Kärcher, B.: Cirrus clouds and their response to anthropogenic activities, Curr. Clim. Chang. Rep., 3, https://doi.org/10.1007/s40641-017-0060-3, 2017.

Kärcher, B. and Corcos, M.: On the lifetimes of persistent contrails and contrail cirrus, J. Geophys. Res., 130, https://doi.org/10.1029/2025JD044488, 2025.

Kärcher, B. and Koop, T.: The role of organic aerosols in homogeneous ice formation, Atmos. Chem. Phys., 5, https://doi.org/10.5194/acp-5-703-2005, 2005.

Kärcher, B. and Marcolli, C.: Aerosol-cloud interactions: the representation of heterogeneous ice activation in cloud models, Atmos. Chem. Phys., 21, https://doi.org/10.5194/acp-21-15213-2021, 2021.

Kärcher, B. and Podglajen, A.: A stochastic representation of temperature fluctuations induced by mesoscale gravity waves, J. Geophys. Res., 124, https://doi.org/10.1029/2019JD030680, 2019.

Kärcher, B. and Ström, J.: The roles of dynamical variability and aerosols in cirrus cloud formation, Atmos. Chem. Phys., 3, https://doi.org/10.5194/acp-3-823-2003, 2003.

Kärcher, B., Jensen, E. J., Pokrifka, G. F., and Harrington, J. Y.: Ice supersaturation variability in cirrus clouds: Role of vertical wind speeds and deposition coefficients, J. Geophys. Res., 128, https://doi.org/10.1029/2023JD039324, 2023.

Kärcher, B., Hoffmann, F., Sokol, A. B., Gasparini, B., Corcos, M., Jensen, E., Atlas, R., Podglajen, A., Morrison, H., Hertzog, A., Plougonven, R., Chandrakhar, K. K., and Grabowski, W. W.: Dissecting cirrus clouds: Navigating effects of turbulence on homogeneous ice formation, npj Clim. Atmos. Sci., 8, https://doi.org/10.1038/s41612-025-01024-w, 2025.

Kim, J.-E., Alexander, M. J., Bui, T. P., Dean-Day, J. M., Lawson, R. P., Woods, S., Hlavka, D., Pfister, L., and Jensen, E. J.: Ubiquitous influence of waves on tropical high cirrus clouds, Geophys. Res. Lett., 43, https://doi.org/10.1002/2016GL069293, 2016.

Koop, T., Luo, B., A.Tsias, and Peter, T.: Water activity as the determinant for homogeneous ice nucleation in aqueous solutions, Nature, 406, https://doi.org/10.1038/35020537, 2000.

Kottayil, A., Podglajen, A., Legras, B., Atlas, R., K, P., Satheesan, K., and S, A.: High-frequency gravity waves and Kelvin-Helmholtz billows in the tropical UTLS, as seen from radar observations of vertical wind, Geophys. Res. Lett., 51, https://doi.org/10.1029/2024GL110366, 2024.

Lamb, D. and Verlinde, J.: Physics and Chemistry of Clouds, University Press, Cambridge, NY, https://doi.org/10.1017/CBO9780511976377, 2011.

L'Ecuyer, P. and Cote, S.: Implementing a random number package with splitting facilities, ACM Transactions on Mathematical Software, 17, 98–111, https://doi.org/10.1145/103147.103158, 1991.

Lemons, D. S.: An Introduction to Stochastic Processes in Physics, The Johns Hopkins University Press, Baltimore, MD, ISBN 978-0-8018-6867-2, 2002.

Lesigne, T., Ravetta, F., Podglajen, A., Mariage, V., and Pelon, J.: Extensive coverage of ultrathin tropical tropopause layer cirrus clouds revealed by balloon-borne lidar observations, Atmos. Chem. Phys., 24, https://doi.org/10.5194/acp-24-5935-2024, 2024.

Lohmann, U. and Kärcher, B.: First interactive simulations of cirrus clouds formed by homogeneous freezing in the ECHAM general circulation model, J. Geophys. Res., 107, https://doi.org/10.1029/2001JD000767, 2002.

Lyu, K., Liu, X., and Kärcher, B.: Exploring sources of ice crystals in cirrus clouds: comparative analysis of two ice nucleation schemes in CAM6, Atmos. Chem. Phys., 25, https://doi.org/10.5194/acp-25-15369-2025, 2025.

Morrison, H., Lier-Walqui, M., Fridlind, A. M., Grabowski, W. W., Harrington, J. Y., Hoose, C., Korolev, A., Kumjian, M. R., Milbrandt, J. A., Pawlowska, H., Posselt, D. J., Prat, O. P., Reime, K. J., Shima, S.-I., van Diedenhoven, B., and Xue, L.: Confronting the challenge of modeling cloud and precipitation microphysics, J. Adv. Mod. Earth Sys., 12, https://doi.org/10.1029/2019MS001689, 2020.

Murphy, D. M. and Koop, T.: Review of the vapour pressures of ice and supercooled water for atmospheric applications, Q. J. Roy. Meteorol. Soc., 131, https://doi.org/10.1256/qj.04.94, 2005.

Nachbar, M., Duft, D., and Leisner, T.: The vapor pressure of liquid and solid water phases at conditions relevant to the atmosphere, J. Chem. Phys., 151, https://doi.org/10.1063/1.5100364, 2019.

Noble, P., Okui, H., Alexander, J., Ern, M., Hindley, N. P., Hoffmann, L., Holt, L., van Niekerk, A., Plougonven, R., Polichtchouk, I., Stephan, C. C., Bramberger, M., Corcos, M., Putnam, W., Kruse, C., and Wright, C. J.: Stratospheric gravity waves in three high-resolution models and AIRS satellite observations, Atmos. Chem. Phys., 26, https://doi.org/10.5194/acp-26-7607-2026, 2026.

Petters, M. D. and Kreidenweis, S. M.: A single parameter representation of hygroscopic growth and cloud condensation nucleus activity, Atmos. Chem. Phys., 7, https://doi.org/10.5194/acp-7-1961-2007, 2007.

Podglajen, A., Hertzog, A., Plougonven, R., and Legras, B.: Lagrangian temperature and vertical velocity fluctuations due to gravity waves in the lower stratosphere, Geophys. Res. Lett., 43, https://doi.org/10.1002/2016GL068148, 2016.

Podglajen, A., Plougonven, R., Hertzog, A., and Jensen, E.: Impact of gravity waves on the motion and distribution of atmospheric ice particles, Atmos. Chem. Phys., 18, https://doi.org/10.5194/acp-18-10799-2018, 2018.

Press, W. H., Teukolsky, S. A., Vetterling, W. T., and Flannery, B. P.: Numerical Recipes in Fortran 77: The Art of Scientific Computing, Cambridge University Press, ISBN 978-0-521-43064-7, 1992.

Randel, W. J. and Jensen, E. J.: Physical processes in the tropical tropopause layer and their roles in a changing climate, Nat. Geosci., 6, https://doi.org/10.1038/ngeo1733, 2013.

Schneider, J., Höhler, K., Wagner, R., Saathoff, H., Schnaiter, M., Schorr, T., Steinke, I., Benz, S., Baumgartner, M., Rolf, C., Krämer, M., Leisner, T., and Möhler, O.: High homogeneous freezing onsets of sulfuric acid aerosol at cirrus temperatures, Atmos. Chem. Phys., 21, https://doi.org/10.5194/acp-2021-319, 2021.

Shinozuka, M. and Deodatis, G.: Simulation of stochastic processes by spectral representation, Appl. Mech. Rev., 44, https://doi.org/10.1115/1.3119501, 1991.

Skrotzki, J., Connolly, P., Schnaiter, M., Saathoff, H., Möhler, O., Wagner, R., Niemand, M., Ebert, V., and Leisner, T.: The accommodation coefficient of water molecules on ice—cirrus cloud studies at the AIDA simulation chamber, Atmos. Chem. Phys., 13, https://doi.org/10.5194/acp-13-4451-2013, 2013.

Uhlenbeck, G. E. and Ornstein, L. S.: On the theory of Brownian motion, Phys. Rev., 36, https://doi.org/10.1103/PhysRev.36.823, 1930.

van Zandt, T. E.: A universal spectrum of buoyancy waves in the atmosphere, Geophys. Res. Lett., 9, https://doi.org/10.1029/GL009i005p00575, 1982.

Wang, M. and Penner, J. E.: Cirrus clouds in a global climate model with a statistical cirrus cloud scheme, Atmos. Chem. Phys., 10, https://doi.org/10.5194/acp-10-5449-2010, 2010.

Wang, P.-H., Minnis, P., McCormick, M. P., Geoffrey, S. K., and Skeens, K. M.: A 6-year climatology of cloud occurence frequency from Stratospheric Aerosol and Gas Experiment II observations (1985-1990), J. Geophys. Res., 101, https://doi.org/10.1029/96JD01780, 1996.

Wilson, R., Pitois, C., Podglajen, A., Hertzog, A., Corcos, M., and Plougonven, R.: Detection of turbulence occurrences from temperature, pressure, and position measurements under superpressure balloons, Atmos. Measurem. Tech., 16, https://doi.org/10.5194/amt-16-311-2023, 2023.

Zhang, C. and Harrington, J. Y.: Including surface kinetic effects in simple models of ice vapor diffusion, J. Atmos. Sci., 71, https://doi.org/10.1175/JAS-D-13-0103.1, 2014.